Contents lists available at ScienceDirect

Applied Surface Science

Full Length Article

Cu metal nanoparticles in transparent electrodes for light harvesting in solar cells

Stefano Boscarino [a,b,*], Valentina Iacono [a,b], Andrea Lo Mastro [a,b], Silvia Scalese [c],
Simona Boninelli [c], Antonino Scandurra [a,b,e], Salvatore Lombardo [c], Roberto Corso [c],
Guglielmo Guido Condorelli [d], Riccardo Reitano [a], Antonio Terrasi [a,b], Maria Grazia Grimaldi [a,b],
Francesco Ruffino [a,b,e]

[a] Dipartimento di Fisica e Astronomia "Ettore Majorana" Università di Catania, Via S. Sofia 64, 95123 Catania, Italy
[b] Consiglio Nazionale delle Ricerche – Istituto per la Microelettronica e Microsistemi (CNR-IMM), Catania-Unit, Via S. Sofia 64, 95123 Catania, Italy
[c] Consiglio Nazionale delle Ricerche – Istituto per la Microelettronica e Microsistemi (CNR-IMM), Catania-Headquartes, Ottava strada n.5, I-95125 Catania, Italy
[d] Dipartimento di Scienze chimiche, Università di Catania, Viale A. Doria 6, 95125 Catania, Italy
[e] Research Unit of the University of Catania, National Interuniversity Consortium of Materials Science and Technology, Viale A. Doria 8 and Via S. Sofia 64, 95125 Catania, Italy

ARTICLE INFO

ABSTRACT

We report on copper nanoparticles produced by laser ablation, in acetone and methanol, from a Cu target using a 1064 nm nanosecond pulsed laser. The morphology, size, structure and chemical composition of the nanoparticles are investigated as a function of the solvent employed. Different analyses confirm the metallic nature of the nanoparticles, without amorphous carbon or copper oxides shells. Then, the nanoparticles are embedded between two transparent electrodes, aluminium-doped zinc oxide (AZO) and zirconium-doped indium oxide (IZrO) as top and bottom layers, respectively. The Glass/IZrO$_{bott}$/Cu nanoparticles/AZO$_{top}$ structures are synthesized and optimized as plasmonic and conductive structure for photovoltaic applications. Optical properties show a strong dependence on the thermal annealing at 200 °C and type of copper nanoparticles embedded in transparent electrodes. The transparent electrode with the lowest E$_{gap}$ limits the E$_{gap}$ to the whole structure. The best structure shows a mean value of transmittance in the visible-NIR range of ~79% with an E$_{gap}$ of 3.43 eV and, moreover, it shows diffused transmittance between 2.5 and 6% in VIS-NIR range and a sheet resistance of 79 Ω/sq. The performances of the best structure are tested measuring the internal quantum efficiency of a tandem solar cell, getting values as high as 89%.

1. Introduction

In recent years, scientific and civil society along with many organizations have pushed for an environmentally sustainable energy transition supported by the development of clean and renewable sources [1–5]. Among these, photovoltaic (PV) technology represents a strategic and well-established choice, offering the potential to directly convert sun-light into electricity. The relevance of the solar cell technology lies in the ability to provide a renewable, sustainable, eco-friendly energy solution that can contribute to reduce greenhouse gas emissions and to contrast the climate changes. A Key factor that has contributed to the widespread adoption of PV technology is the considerable reduction in the cost of the PV modules. In the last decade, thanks to the

advancements in manufacturing processes, economies of scale and improvements in solar cell efficiency, there has been an impressive decrease, of about 82%, in the global cost of photovoltaic energy production, making it competitive with conventional energy sources [1]. Key process to increase the solar cell efficiency involves the absorption of light, which generates electron-hole pairs leading to the electrical current production in external circuits. Enhancing the efficiency of light absorption, also known as light harvesting, is of fundamental importance to improve overall solar cells performance. Conventionally, textured surfaces have been employed to reduce the light reflection and to increase the path length of light within the absorber layer, by introducing random or inverted pyramid structures [6–10]: the sun-light scatters over a wide angular range increasing its path length inside the

---

absorber material. While this approach has shown some success, on the other hand it presents issues and limitations [6], therefore researchers have actively been exploring alternative approaches. The advent of nanoscience and nanotechnology in the 21st century, has revolutionized various scientific disciplines such as photonics, optoelectronics, biosensors, and also the field of photovoltaics has benefitted significantly [6,11–14]. Particularly, metal nanostructures have gained significant attention due to their unique physical–chemical properties, which arise from their small dimensions and large surface to volume ratio. One of the most notable properties of metal nanostructures, among many others, is the surface plasmon resonance (SPR). SPR phenomenon takes place when the size of the nanostructures becomes smaller, or comparable, than the wavelength λ of incident light. The free electrons in the metal, in this condition, collectively oscillate in resonance as response to the electromagnetic radiation, leading to the formation of SPR. When SPR becomes localized at the surface of the nanostructures, it is referred to as localized surface plasmon resonance (LSPR) [15–17]. When the incoming sun-light hits the nanostructures, it couples with the localized surface plasmons, leading to strong absorption and/or scattering of sunlight. The increased interaction with sunlight significantly enlarges the optical path length inside the PV absorber material, resulting in higher efficiency of sunlight-to-electricity conversion. Therefore, harnessing LSPR opens up a new route to enhance light harvesting performance of solar cells. To fully take advantage of a metal nanostructure in solar cells, several factors need to be considered such the type of metal, the shape and size, the spacing between the nanostructures and the dielectric properties of themselves and surrounding medium. These factors influence the intensity and wavelength position of the LSPR, therefore their optimization is critical to achieve the desired light harvesting performance of solar cell.

The optical response of single and a system of nanoparticles has been studied with several analytic or semi analytic methods as a function of the nanoparticle diameter d: e.g. quasistatic approximation ($d \ll \lambda$, $10 < d < 100$ nm), Mie-theory ($d < 10$ nm or $d > 100$ nm) [17]. For a sphere of volume V and dielectric function ε, in the quasi-static limit, the extinction cross section is given by the sum of absorption and scattering cross section: $\sigma_{Extinction} = \sigma_{Absorption} + \sigma_{Scattering}$ [15,17].

To date, gold and silver noble metals have been extensively studied and used for their excellent plasmonic properties, but they come with a drawback of high cost limiting large-scale production and commercialization. As an interesting alternative, copper has emerged as a promising candidate due to its earth-abundant nature and significantly low cost, \$0.008/g for Cu vs to \$0.74/g for Ag and \$61.66/g for Au [18–20]. Despite its potential, copper has faced challenges related to rapid oxidization and other drawbacks, leading to a weak and broad LSPR response at about 590 nm. Researchers have proposed various techniques and technological solutions in order to overcome this limitation. Some of these solutions are the use of different Cu nanostructure shapes, such as Cu nanocube [20], Cu half-shell [21] and nanotriangle shapes [22]. Moreover, methods like solid-state dewetting, nanosphere lithography, e-beam lithography, and laser ablation, or wet processes have been explored to achieve a more intense and narrow LSPR peak [20–30]. Furthermore, non-aqueous solvents such as ethanol, glycol, and acetone have been proposed to prevent copper oxidation in the preparation processes of nanostructures by laser ablation [28–30]. Alternatively, the inclusion of copper nanostructures into different matrices has been proposed [31–35]. Among the matrices, aluminum-doped zinc oxide (AZO) and Zirconium- doped Indium Oxide have proven to be excellent embedding materials, with compatibility for solar cell manufacturing and indium-free (or very low indium content) alternative for transparent electrodes or buffer layers [34–37].

In our previous works [34,35], we focused on Solid-State Dewetting (dry method) and laser ablation of copper solid target in acetone, methanol or IPA (wet method) to produce copper nanoparticles (Cu NPs) which, in turn, were embedded between two layers of transparent and conductive oxides (TCOs) of AZO (aluminum-doped zinc oxide), IZrO

(Zirconium-doped Indium oxide) with all combinations of AZO and IZrO as top and bottom layers. In particular, the position of the SPR peaks, related to wet Cu NPs, were at 610 nm, 580 nm and 578 nm for acetone, IPA and methanol respectively [34,35]; and these TCOs were selected, for the motivations previously mentioned. Among the dry physical methods, solid-state dewetting (SSD) offers cost effective, time efficient solutions and is fully compatible with the industrial manufacturing lines of solar cells, especially for thin film photovoltaics. Wet physical methods like laser ablation of solid target in liquid medium (LAL) offer advantages such as simplicity of operation, environmentally friendly technique, operating under ambient conditions in water or organic liquids and a limited equipment requirement. The most expensive elements of the LAL setup are the laser system and the target material employed. In LAL process a laser beam is focused, by optical lens, on the surface of a solid target, immersed in a solvent, which absorbing the laser radiation, and under suitable condition, leads to the nucleation and growth of metal particles. Then, the nanoparticles are released into the surrounding solvent, hence, forming a nanoparticle colloidal suspension [38]. Different key factors determine the resulting morphology of nanostructures such as laser wavelength, pulse duration, laser fluence, repetition rate and the liquid environment where the ablation was executed.

The goal of these works was the fabrication of a structure TCO$_{bott}$/Cu NPs /TCO$_{top}$ to achieve a plasmonic and conductive structure (PCS) for photovoltaic applications. This was done by comparing the involved methods of Cu NPs synthesis and all produced structures. We studied the evolution and modification of the electro-optical properties of PCS as a function of the type, dimension and shape of Cu NPs (by wet or dry method), the thickness of both TCOs and copper (for SSD method) and the dependence on the sequence of the top and bottom TCOs deposited. The PCSs showing the best electro-optical performances, were made of Glass substrate/IZrO$_{bott}$/ wet Cu NPs/AZO$_{top}$.

In this work, based on previously researches, Cu nanoparticles are produced by wet Laser ablation in liquid of Cu target, using a 1064 nm nanosecond pulsed laser in acetone and methanol. The morphology, size, structure and chemical composition of the NPs are investigated as a function of the used liquid environment by means of Scanning Electron Microscopy (SEM), High Resolution Transmission Electron Microscopy (HR-TEM), Energy Dispersive X-Ray (EDX) and Electron Energy Loss Spectroscopy (EELS) in Scanning Transmission Electron Microscopy (STEM) configuration, X-ray Diffraction (XRD) and X-ray photoelectron spectroscopy (XPS). These different analyses confirm the metallic nature of Cu NPs produced by LAL process. Then, the produced Cu nanoparticles were embedded in a mix of transparent electrodes with AZO and IZrO as top and bottom layers, respectively. The Glass/IZrO$_{bott}$/ wet Cu NPs/AZO$_{top}$ structures were synthesized and further optimized with the aim to create a plasmonic and conductive structure for photovoltaic applications.

Wet PCS by a thermal annealing at 200 °C for 30 min in N$_2$ atmosphere can achieve sheet resistance of about 79 Ω/sq. Optical properties such as energy band gap (E$_{gap}$), absorbance, direct and diffused transmittance, and specular and total reflectance are investigated in 250–1100 nm wavelength range.

They show a strong dependence on the thermal annealing and type of wet Cu NPs embedded in transparent electrodes. The transparent electrode with the lowest E$_{gap}$ limits the E$_{gap}$ to whole PCS. The Best PCS, made with Cu NPs produced in acetone, showed a mean value of transmittance in Vis-NIR range of ∼ 79 %, an E$_{gap}$ of 3.43 eV and, moreover, a diffused transmittance, between to 2.5–6% in VIS-NIR range. Finally, the performances of our best PCS are tested measuring values as high as 89 % for the Internal Quantum Efficiency of a tandem Si solar cell (a-Si:H/c-Si) where our best PCS was deposited on top.

2. Experimental section and methods

RF magnetron sputtering was employed to deposit AZO thin film on

Corning glass 2947, the following deposition parameters were used: power density of 2.16 W/cm^2 on ceramic AZO target (2 wt% Al$_2$O$_3$, 98 wt% ZnO), distance between target and substrate of 7 cm, room temperature deposition and argon atmosphere with a working pressure of $5.7\ 10^{-3}$ mbar. The deposition time was set at 5 min in order to achieve a thickness of about 85 nm.

IZrO thin film was obtained by RF and DC magnetron co-sputtering technique, employing a Zirconium target (Zr – 99.99% purity) and In$_2$O$_3$ target (99.99 % purity). The parameters of the co-sputtering deposition were: power density of 8.86 W/cm^2 for In$_2$O$_3$ (in RF mode), power density of 11.22 W/cm^2 for Zirconium (in DC mode), room temperature deposition and argon atmosphere with a working pressure of $1.6\ 10^{-2}$ mbar. The deposition time was set at 60 min in order to achieve a thickness of about 65 nm. The co-sputtering deposition was performed in a sputter-up configuration along with a rotating sample holder.

The copper nanoparticles (Cu NPs) were produced by means of pulsed laser ablation of a Cu metal target (1.0 mm thick, 99.99 purity) immersed in 8 ml of acetone or methanol solvent. Nd:YAG laser (Spectra Physics, Santa Clara, CA, USA) was employed for the laser ablation using the following parameters: $\lambda = 1064$ nm, 10 Hz frequency, 10 ns pulse, mean output power of 5 W and 8 min ablation time. A laser spot of 2 mm was focused with a 100 mm focal length lens on the copper target placed at the bottom of a teflon vessel filled with acetone or methanol. The Cu nanoparticles were transferred from the colloidal suspension onto the surface of bottom TCO by drop-casting method.

Thermal annealing on PCS alone and Tandem a-Si:H/c-Si solar cells with PCS on top was carried out by means of a tubular oven made by Carbolite Gero in a satured N$_2$ atmosphere (in order to avoid spontaneous oxidation) at 200 °C for 30 min.

Morphological characterization was performed by Scanning Electron Microscopy (SEM), employing a Supra35 Field Emission – SEM by Zeiss (Oberkochen, Germany). The analyses were performed with an acceleration voltage of 3 kV, 3 mm working distance, in-lens detector with a standard aperture size of 30 μm.

The suspension containing the ablated Cu NPs in liquids (acetone or methanol) were sonicated for 10 min and drop-casted on Au C-lacey TEM grid. The morphology was investigated by using a 200 keV Jeol JEM 2010F microscope. More detailed structural analyses were performed via Scanning Transmission Electron Microscopy (STEM) in High Angle Annular Dark field (HAADF-STEM) mode by using a Jeol ARM 200F microscope (at 200 keV) equipped with a probe aberration corrector. Compositional analyses were performed by employing Electron Energy Loss Spectroscopy (EELS) and Energy Dispersive X-Ray (EDX) analyses in spectrum imaging (SI) mode. This allows to correlate the spatial information with the chemical composition in one single pixel. EELS and EDX spectra were, respectively, integrated in a region including the individual nanoparticles to obtain a spectrum carrying not only information of the chemical elements composing the sample, but also their spatial distribution.

Surface chemical composition of Cu nanoparticles produced in acetone or methanol were studied by X-ray Photoelectron Spectroscopy (XPS). For the analysis, the nanoparticles were supported on a Si substrate by drop-casting the respective suspensions. Measurements were carried out by PHI 5000 VersaProbe II equipped with a monochromatic Al Kα X-ray source of 1486.6 eV. The base pressure of the analysis chamber was in the range of 10^{-10} mbar. Peak fitting of Cu 2p and C 1 s was done by 20% Lorentzian – 80 % Gaussian and 100% Gaussian components, respectively, after linear background subtraction. The binding energy scale was calibrated on the C 1 s peak at 285.0 eV. Samples were prepared by drop casting of μl of colloidal suspension on silicon substrate and letting it dry on a hot plate.

X-Ray Diffraction (XRD) measurements were performed using a Smartlab Rigaku diffractometer working in Bragg-Brentano mode and equipped with a rotating anode of Cu Kα radiation operating at 45 kV and 200 mA. Bragg–Brentano patterns were acquired with a resolution

step of 0.02°. Samples were prepared by drop casting of a large amount of colloidal suspension (less than 1 ml) on a Corning glass substrate.

The surface roughness of film was observed by Atomic Force Microscopy (AFM-Bruker-Innova microscope - Billerica, MA, USA). The AFM images were analyzed by using the SPMLABANALYSES V7.00 software to extract values for the RMS (Root Mean Square) of the films surface.

The sheet resistance (R_{sh}) of all structures was measured at room temperature by a four-point collinear probe method using a Keithley 4200 semiconductor characterization system. Moreover, R_{sh}, Hall mobility μ_e, and carrier concentration n_e were measured by a 4-point probe in the Van der Pauw configuration, at room temperature, by a Hall Effect Measurements System HL5500PC.

The optical properties of direct transmittance (T_{dir}), specular reflectance (R_{spec}) and absorbance (Abs) spectra of samples were measured by means of a Varian Cary 500 double-beam scanning UV–vis-NIR spectrophotometer in the range 250–1100 nm. The specular reflectance was measured in specular geometry at 20° (using a silicon-calibrated sample as reference), the direct transmission spectra was normalized to 100% baseline obtained using an empty sample holder. The direct transmittance (T_{dir}), diffused transmittance (T_{diff}), total Reflectance (R_{tot} = specular reflectance + diffused reflectance) were measured using a UV/Vis-NIR spectrometer Perkin Elmer Lambda 1050 + equipped with an integrating sphere. All the optical data included the glass substrate's contribution.

2.1. Wet PCS preparation

The TCO$_{bott}$/Cu NPs/TCO$_{top}$ structures (PCSs) in wet configuration, Fig. 1a), were produced in four sequential steps. The first step (1st step) was the deposition, by sputtering, of the bottom IZrO thin film on the glass substrate, then the deposition of the Cu NPs (2nd step) on bottom IZrO layer and the deposition of the top AZO layer (3rd step) in order to cover and protect the Cu NPs.

The deposition of Cu NPs onto IZrO was preceded by an ultrasonic dispersion process, on the colloidal suspension, in order to avoid the agglomeration of Cu NPs. An aliquot of 100 μl of suspension was poured onto the IZrO bottom layer. Acetone or methanol were evaporated by means of hot plate at 100 °C for 15 min. This step involved the glass substrate/IZrO$_{bott}$/ Cu NPs stack. After the evaporation of the solvent, the top AZO layer was deposited. Finally (4th), the structure glass substrate/IZrO$_{bott}$/Cu NPs/AZO$_{top}$ was subjected to a thermal annealing @ 200 °C, in N$_2$ atmosphere, for 30 min. For reference also a double stack Glass/IZrO$_{bott}$/AZO$_{top}$ were produced, as deposited (as dep.) and after the same thermal treatment carried out on PCS. The only difference between the PCS and the double stack was in the presence and absence of Cu NPs respectively, the other deposition and manufacturing parameters were the same.

2.2. PCS on solar cell & EQE/IQE characterization

The PCS (or double stack) was deposited on tandem solar cell made by: a-Si(p$^+$):H/a-Si(i):H/c-Si(n)/a-Si(i):H/a-Si(n$^+$):H/Aluminum film. The performance of solar cell with PCS or double stack, as deposited or after the thermal annealing, were tested by external quantum efficiency (EQE) measurements with Bentham - PVE300 Photovoltaic EQE and IQE solution. The system was also equipped with an integrated sphere to measure the total reflectance in order to convert the EQE to internal quantum efficiency (IQE). The processes and deposition parameters of PCS and double stack on solar cell were the same of "Wet PCS preparation" but the deposition sequence of transparent electrodes was inverted because of PCS was on front of solar cell, Fig. 1a) and b). The sun-light after has passed through the glass hits the PCS deposited on the tandem junction. The PCS or double stack was deposited on a-Si(p$^+$):H. The EQE measurement was performed to illuminate the front side of solar cell (20 × 20 mm^2) under a constant irradiance of 1000 W/m^2 with
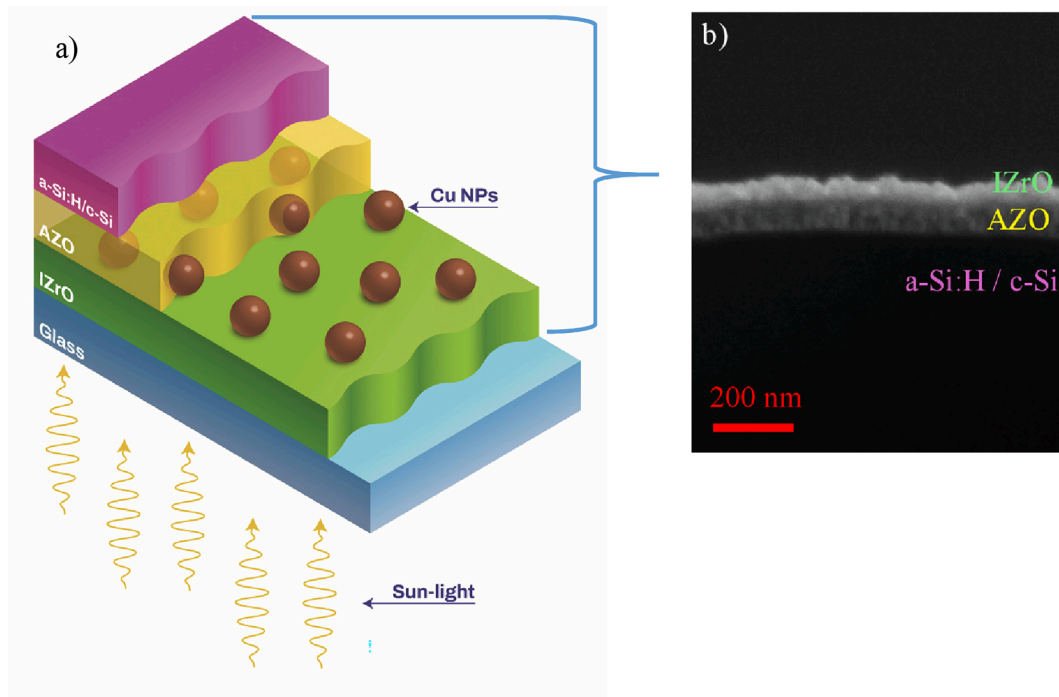
Fig. 1. a) Illustration of AZO and IZrO transparent electrodes with Cu NPs (in acetone or methanol) used to fabricate the wet PCS, the latter is in contact to tandem Si solar cell. b) SEM image of PCS deposited on tandem Si solar cell.

AM1.5G spectrum and with a sample temperature maintained at 25 °C. The wavelength was varied from 300 to 1100 nm with a step of 5 nm. A c-Si reference solar cell was used for the calibration of the EQE detection system.

3. Results and discussions

3.1. Morphological, structural, compositional and size characterizations

SEM and HR-TEM analysis were performed to obtain morphological, size distribution and structural informations on Cu NPs produced in acetone and methanol.

Fig. 2a) and figure S1 a), show Cu NPs produced in Acetone at different magnifications. As we can see a lot of NPs were widely distributed on the substrate, some NPs had size close to SEM resolution and, in particular, in high magnification image they showed a spherical shape. A detailed inspection revealed both large nanoparticles and small nanoparticles, like in acetone, where some of the larger ones were the agglomeration of two or more particles with a non-perfect spherical shape.

Size distribution analysis on Cu nanoparticles was performed via ImageJ software [39], setting a brightness threshold and using the automated algorithm of the software that counted about 1000 nanoparticles: that was done thanks to the clear contrast between the nanoparticles and the substrate. Another threshold was set on the dimension, because particles smaller than 15 nm (radius) were barely visible. A check to verify the accuracy of the algorithm result was done by observing and measuring one by one the Cu nanoparticles that appeared visible. The nanoparticles distribution of Cu NPs in acetone, Fig. 2b), showed a log-normal trend, in agreement with the literature on Pulsed Laser Ablation in Liquid -based NPs Production [38]:

$$f(x) = \frac{1}{xw\sqrt{2\pi}} exp^{\left(-\frac{ln^2(x/x_c)}{2w^2}\right)} \qquad (1)$$

where x_c is the median of the distribution and w is the scale parameter related to the distribution width. The peak value (the distribution mode) is given by $x_p = exp^{\left(ln(x_c)-w^2\right)}$, while the mean value is given by $x_m = exp^{\left(ln(x_c)+w^2/2\right)}$. A geometric standard deviation can be defined as.

$$\sigma = ln(w) = \sqrt{\left(\sum_i n_i (ln(x_i) - ln(x_c))^2\right)\Big/\sum_i n_i}.$$ The distribution is not symmetric, so these two parameters will be reported from now on instead of mean and standard deviation. The distribution is the statistical result of the multiplicative product of many independent random positive variables, and so f(x) goes to zero with the radius x [40]. For these nanoparticles, the statistical analysis showed a large amount of small particles and few bigger ones. The fitted distribution curve reports $x_c = 16$ nm and $w = 0.2$ with the most representative value $x_p = 15$ nm.

For Cu nanoparticles produced in methanol, size distribution analysis, once again, follows a log-normal distribution: the fitted distribution curve reported $x_c = 47$ nm, $w = 0.67$, and the most representative value is $x_p = 31$ nm. More detailed morphological and structural information on Cu nanoparticles, not accessible by SEM, were obtained by TEM analysis. The method used for analyzing the size distribution of the nanoparticles was the same described previously, and applied to TEM images of Cu nanoparticles made in acetone and methanol. High resolution TEM also provides information on the crystallinity of the nanoparticles.

Fig. 2c) and figure S1 b) show TEM images, at different magnifications, of the Cu nanoparticles in acetone, while Fig. 2d) reports the size distribution with the Log-Normal fit curve. As a result, the values of the two fit parameters and the most representative value of the nanoparticles radius are: $x_c = 2.9$ nm, $w = 0.5$ and $x_p = 2.7$ nm.

Fig. 2g) and figure S1 d) show TEM micrographs of the Cu nanoparticles in Methanol, while Fig. 2h) reports on the size distribution with the log-normal fit curve. As a result, the values of the two fit parameters and the most representative value of the nanoparticles radius are: $x_c = 2.1$ nm, $w = 0.6$ and $x_p = 1.7$ nm. These results have also been supported by means of a Monte Carlo approach, for the evaluation of nanoparticles size distribution from an optical analysis [41].

Therefore, TEM images and relative size distributions, for both Cu NPs in Acetone and Methanol, allowed to observe the existence of Cu

Cu NPs in acetone

Cu NPs in Methanol
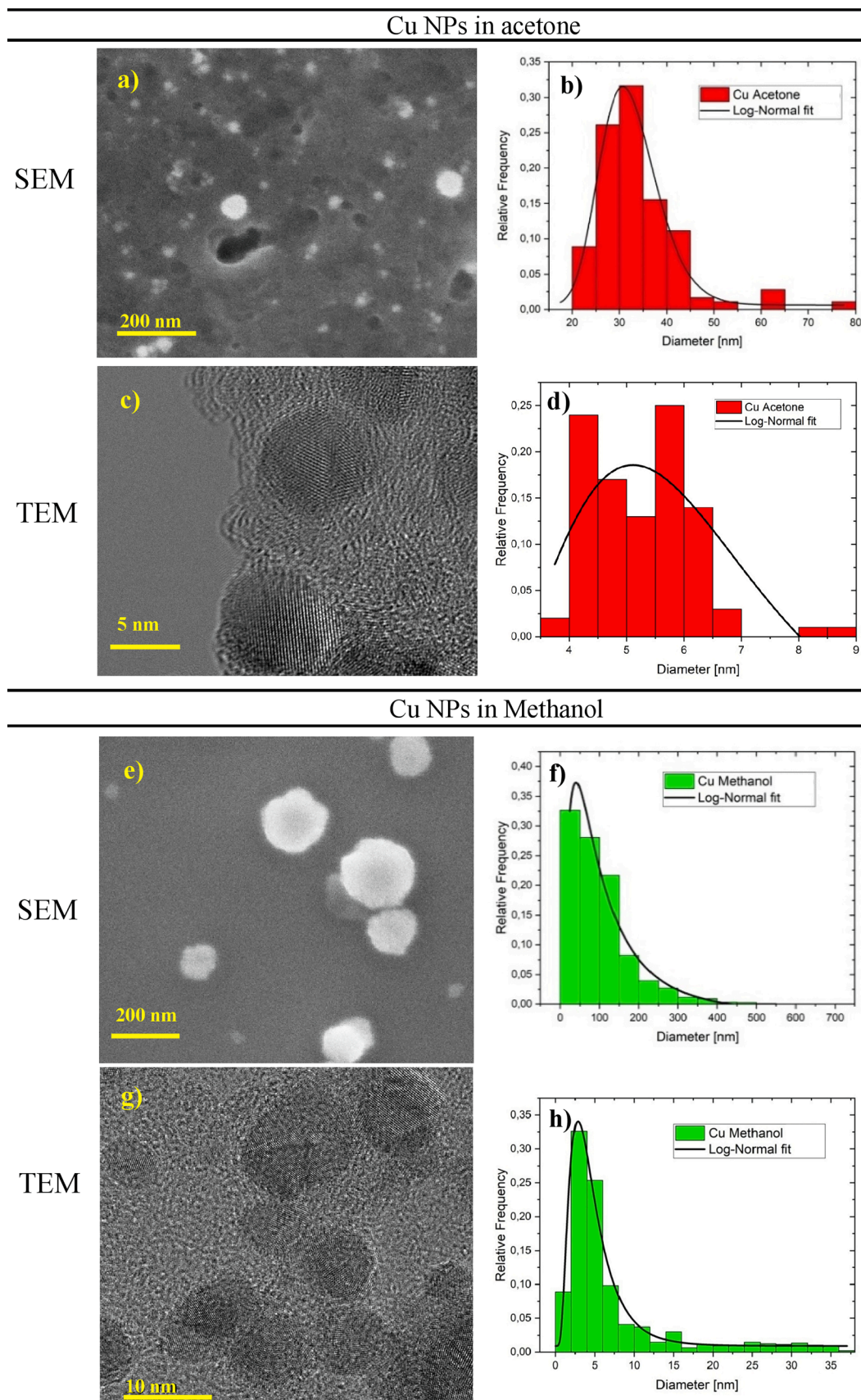
Fig. 2. SEM, a), and TEM, b), images of the Cu nanoparticles produced in acetone and their relative size distribution with a Log-Normal fit b),d). SEM, e), and TEM, g), images of the Cu nanoparticles produced in methanol and their relative size distribution with a Log-Normal fit f),h).

nanoparticles ten times smaller than those observed via SEM.

In addition, a very important information can be obtained from this detailed TEM analysis, see Fig. 2c) and Fig. 2g): Cu nanoparticles do not present amorphous carbon or copper oxides shells (further analysis, as shown below, confirm this assertion) and present crystalline structures, as pointed out by the clearly resolved crystalline planes. Some of them present defects in their structure such as twin dislocations, a clear sign of the strongly out-of-equilibrium process that took place during laser ablation.

XPS analysis was carried out to investigate the chemical composition and the electronic structure of surface of the copper nanoparticles. Figure S2 a)-b) show the survey spectra in the range 0–1200 eV of binding energy of Cu NPs produced in acetone and methanol, respectively. Both spectra show the signals of Cu, O and C. Moreover, weak signals of Si can be observed in the spectrum of the Cu NPs produced in methanol, due to the substrate. Fig. 3 shows the Cu $2p_{3/2}$ and C 1 s spectral regions of Cu NPs produced in acetone (a,b) and methanol (c,d), respectively. Both Cu 2p spectra can be deconvoluted by two components centered at 933.5 eV and 935.5 eV that can be assigned to Cu(II) species coordinate by R-COO$^-$ and R-COO$^-$/OH$^-$ specie via oxygen bonds, respectively [42,43]. Noteworthy, the peak of the sample obtained in acetone shows a greater intensity of the component at binding energy of 935.5 eV (35%) compared to that of sample obtained in methanol (28%).

The shake up bands between 940 and 945 eV, assigned to open $3d^9$ shell, confirm the presence of Cu(II) specie. Interesting, the corresponding C 1 s spectra confirm the assignments done. In particular, the C 1S spectra can be deconvoluted by four components centered at 285.2, 286, 287.3 289.1 eV (acetone) assigned to C*-C/C*-H, R-C*H$_2$-OH, R (C*=O)-R, R-(C*O)O$^-$ functional groups, respectively, and 285.6, 287 and 289 eV (methanol) assigned to R-C*H$_2$-OH, R(C*O)-R', R-(C*=O)O$^-$ [42,43]. All these groups are likely present in a shell that envelops and coordinates the Cu NPs and can be ascribed to an unconventional rearrangement and a partial polymerization of the solvents molecules occurring under laser irradiation. The component at 285 eV is absent in

the spectrum of methanol, this finding may reflect the different chemical structure between acetone and methanol.

Further investigations by XRD, EELS and EDX in STEM configuration were carried out in order to support this result.

More details about the structural properties of the Cu nanoparticles were obtained XRD technique.

Fig. 4a) and Fig. 4b) show the XRD diffraction patterns of Cu NPs produced in acetone and methanol respectively, with reference values (and their relative intensities) for metallic copper.

As evident in the XRD pattern, the experimental peaks of Cu NPs fit very well with reference peaks; in particular, for both XRD patterns, there are three strong peaks at ~ 43.30°, 50.43° and 74.13°. These last ones coincide with the significant peaks associated to the crystalline planes of metallic fcc Cu, identified by Miller indices (1 1 1), (2 0 0) and (2 2 0), respectively [44].

In addition, reference peaks of Cu oxides [45,46], i.e. CuO and Cu$_2$O (not reported), are compared with experimental peaks and none of the reference peaks coincide with those present in both XRD patterns. Therefore, some apparent (less intense) peaks in both XRD patterns are considered background noise. The results obtained from XRD measurements confirm the previous hypothesis on the metallic nature of nanoparticles with no others impurities observed.

Further chemical and compositional analyses were carried out on Cu NPs. In particular, Electron Energy Loss Spectroscopy (EELS) analysis was employed for Cu NPs in acetone, Fig. 5, and Energy Dispersive X-ray (EDX) analysis for Cu NPs in Methanol, Fig. 6.

EELS spectrum, Fig. 5b), and its high-loss region, inset in Fig. 5b), present different edges related to carbon, oxygen and copper. Carbon signal is due to acetone and carbon lacey (support of the sample), the large amount of carbon in the sample, Fig. 5c), is related to acetone that reacts with carbon lacey incorporating it. Copper (green) is exclusively present within the nanoparticles, according to Fig. 5c)-d).

Oxygen (red), due to solvent, shows a random distribution in the sample, therefore we can state it is not inside the nanoparticles as oxidizing element but only in the solvent surrounding Cu nanoparticles,
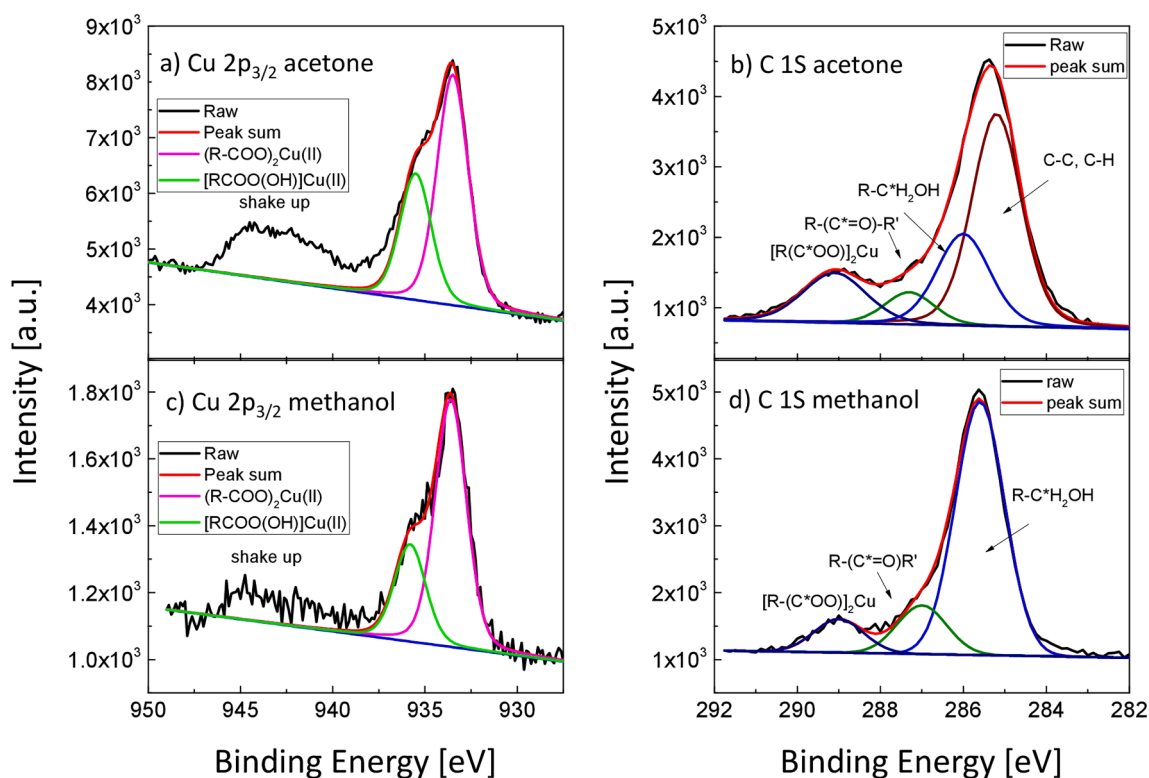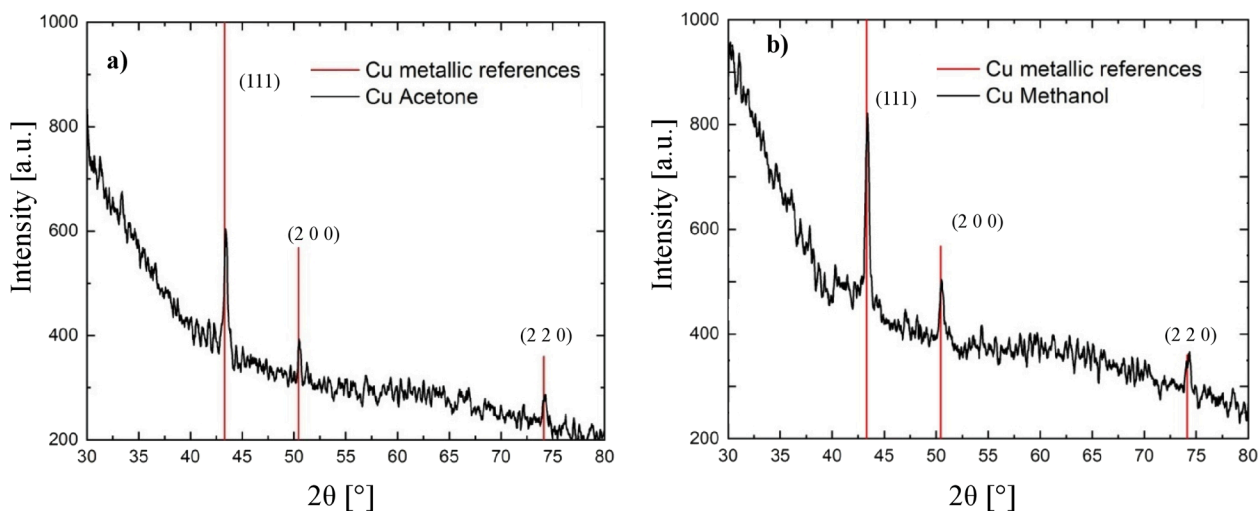

Fig. 3. XPS spectra of: a) Cu $2p_{3/2}$ and b) C 1S of the Cu NPs prepared in acetone; c) Cu $2p_{3/2}$ and d) C 1S of Cu NPs prepared in methanol, with references.

Fig. 4. XRD pattern of Cu nanoparticles in acetone (a) and in methanol (b) solvents deposited on Corning Glass. The reference data for metallic Cu (red lines) is reported with their relative Miller indices. (For interpretation of the references to colour in this figure legend, the reader is referred to the web version of this article.)
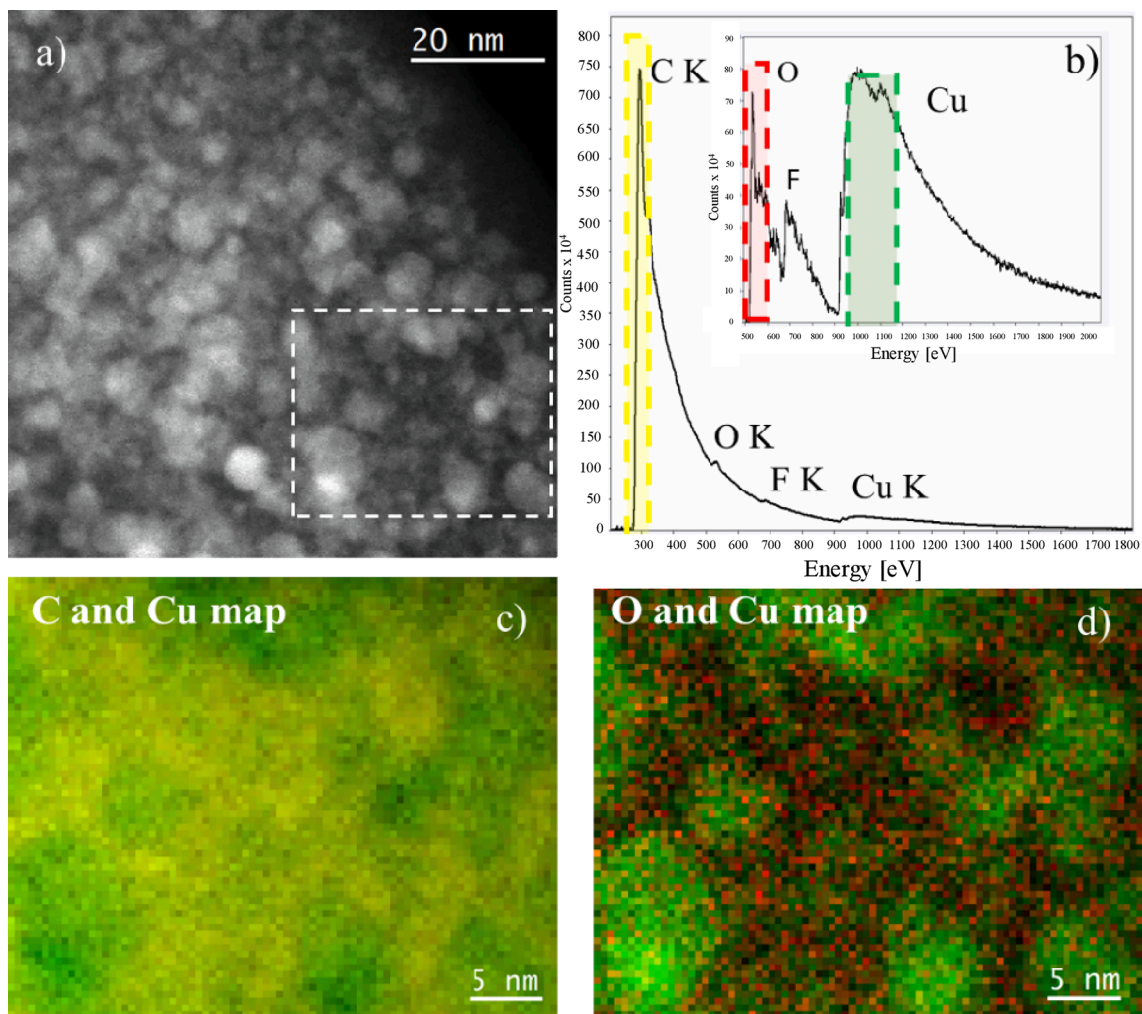
Fig. 5. (a) STEM image of Cu NP in Acetone. (b) EELS spectrum of the selected region in (a). Insert: High-loss region showing O and Cu peaks. (c) C (yellow) and Cu (green) map and (d) O and Cu EELS map from the selected region in a). (For interpretation of the references to colour in this figure legend, the reader is referred to the web version of this article.)
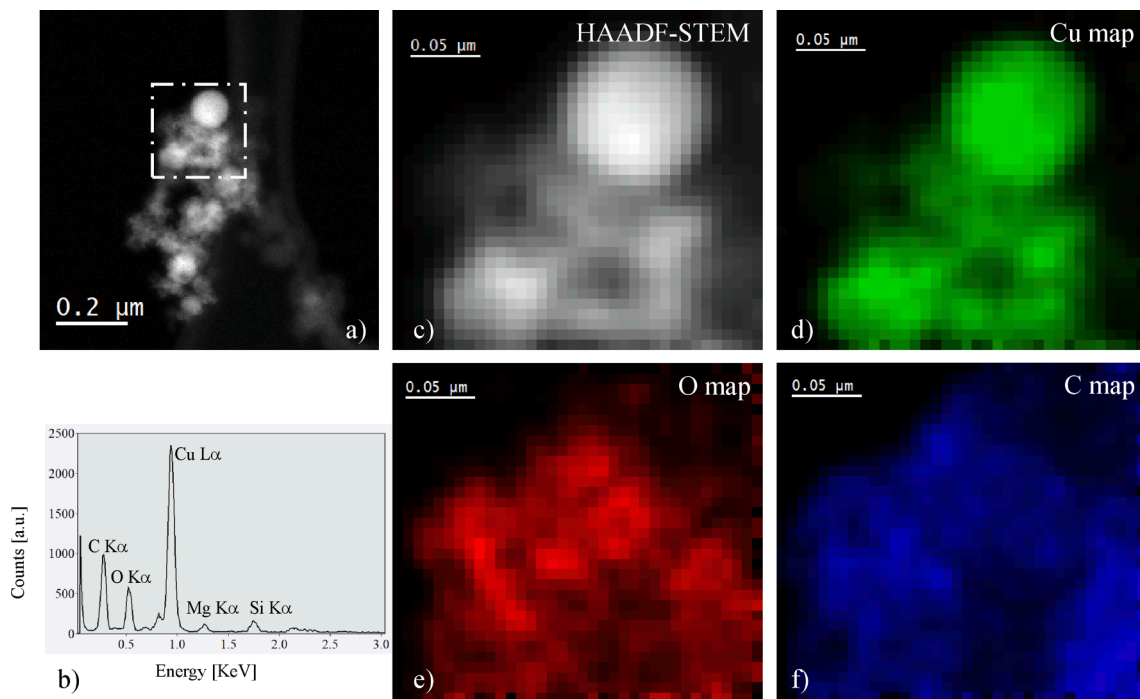
Fig. 6. (a) STEM Z-contrast image of Cu cNanoparticles in Methanol. (b) EDX spectrum acquired in correspondence of the selected region. (c) Scanning Transmission Electron Microscopy in High Angle Annular Dark field image. EDX chemical maps of Cu (d), Oxygen (e) and Carbon (f), respectively.
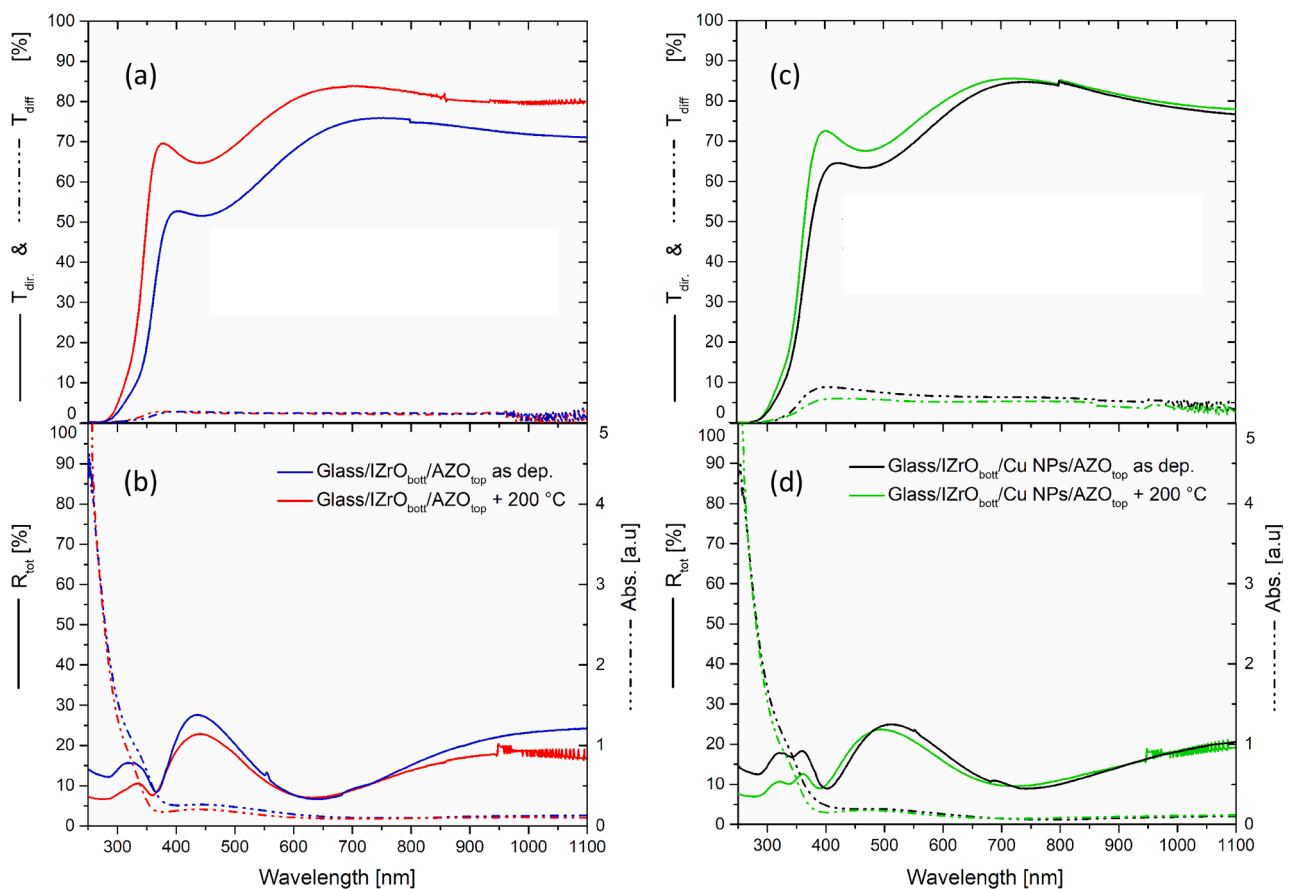
Fig. 7. direct transmittance, diffused transmittance, total reflectance and absorbance curves of Glass/IZrO$_{bott}$/AZO$_{top}$, as deposited and after a thermal annealing a) and b), and Glass/IZrO$_{bott}$/Cu NPs in acetone/AZO$_{top}$, as deposited and after a thermal annealing c) and d).

Fig. 5d). Fluorine signal relates to a contaminant from the solvent or vessel used for the laser ablation process. Regarding Cu NPs in Methanol, Fig. 6 show EDX analysis (STEM configuration) with chemical maps.

Fig. 6a)-c) show a STEM Z-contrast and HAADF-STEM image of a selected region, where different Cu nanoparticles are investigated with the corresponding EDX spectrum, Fig. 6b). The EDX spectrum shows an intense copper peak with respect to C and O, although some impurities, like Mg and Si, are detected too. Looking at the chemical maps in Fig. 6 d), e) and f), copper (green) is only present within the nanoparticles, while carbon (blue) and oxygen (red) are distributed uniformly outside the NPs, in the carbon lacey of TEM grid. Interestingly, the NP on top is highly brilliant because it is composed by Cu, without any spurious contribution of oxygen and carbon. The combined maps of Cu–O and C-O reported in figure S3 a)-b) put clearly in evidence the absence of C and O contribution in the Cu NP. In conclusion, these analysis highlight that the nanoparticles are made of metallic copper, without any shell, and they overlapping in the oxidized C lacey film.

3.2. Electro-optical properties of Glass/IZrO_bottom/wet Cu NPs/AZO_top

In our previous works, as mentioned before, we studied the evolution and modification of the PCS electro-optical properties as a function of the type, dimension and shape of Cu NPs created by wet or dry method, the thickness both TCOs and copper (only for SSD method) and the dependence on the sequence of the top and bottom TCOs deposited [34,35]. Based on these researches, here, with the aim of further improve the PCS, we focused only on "wet" Cu NPs produced in acetone and methanol and in a PCS based on IZrO and AZO layer as bottom and top transparent electrodes respectively. Comparing the effects on electro-optical properties of wet Cu produced in acetone e methanol inside the same outer transparent electrodes, one more time, observed that wet Cu NPs produced in acetone showed best electro-optical performance than Cu NPs in methanol (see figure S4), especially after a thermal treatment of 200 °C, 30 min, in saturated N_2 atmosphere. For this reason why we focus on and show the electro-optical of PCS made of Glass substrate/IZrO_bott/ wet Cu NPs Acetone/AZO_top.

Fig. 7 shows the direct and diffused transmittance, total reflectance and absorbance spectra of the double stack Glass/IZrO_bott/AZO_top, as deposited (as dep.) and after a thermal treatment, as well as the PCS Glass/IZrO_bott/Cu NPs in acetone/AZO_top, as dep. and after the thermal treatment. The optical behaviours of the double stack as dep. and after the annealing were fundamental as reference in order to compare and understand the optical properties of wet PCS, both as dep. and after the annealing.

As we can observe, the presence of Cu NPs between the transparent electrodes improved the transmittance respect to the double stack: in particular we can achieve a diffused transmittance between 3 and 9.5 % in the range 350–1100 nm compared to the double stack exhibiting values between about 1–2.5 %, as expected for this very thin system. The higher values of light scattering were achieved in the visible range. At the same time, the PCS showed higher direct transmission than the double stack, thanks to the presence of Cu NPs. The thickness of transparent electrodes (with the presence of Cu NPs) was optimized in order to adjust the interference phenomena that occur at the interfaces, so as to maximize the transmittance and minimize the reflectance [47]. After a thermal annealing at 200 °C for 30 min, we observed that in the PCS the direct transmittance improved, mainly in the visible and near UV, while the diffused transmittance decreased down to values between 2.5 and 6 % in visible-NIR range. On the other hand, the double stack after the annealing improved much from near UV to NIR, while the diffused transmittance showed slight reduction in the visible-NIR range, down to less than 1% in IR. After the thermal treatment the double stack and the PCS achieved mean values of direct transmittance in the visible range and visible- NIR range of $<T>_{Vis} = 76.3$ %, $<T>_{Vis-NIR} = 78.2$ % and $<T>_{Vis} = 78.0$ %, $<T>_{Vis-NIR} = 79.2$ %, respectively. See Table 1 for more details on mean values of transmittances, in Vis and Vis-NIR range,

Table 1

Comparison of sheet resistance, R_{sh}, energy band gap, E_{gap}, mean value T in Visible (400–800 nm), $<T>_{Vis}$, and Vis-NIR (400–1100 nm), $<T>_{Vis-NIR}$, of Glass/IZrO_bott/AZO_top and Glass/IZrO_bott/Cu NPs in acetone/AZO_top as deposited and after the thermal annealing.

Samples	R_{sh} [Ω/Sq]	E_{gap}	$<T>_{Vis}$ (%)	$<T>_{Vis-NIR}$ (%)
IZrO_bott/ AZO_top	236	3.38	65.4	68.5
IZrO_bott/AZO_top + 200 °C	83	3.57	76.3	78.2
IZrO_bott/Cu NPs /AZO_top	253	3.39	74.7	76.9
IZrO_bott/ Cu NPs/AZO_top + 200 °C	79	3.43	78.0	79.2

before and after the thermal annealing.

The absorbance spectra of the double stack and PCS were very low in the visible-NIR, and decreased after the thermal treatment. For the high absorption in UV range, for both samples, before and after the thermal treatment, is related to the energy band-gap (E_{gap}) of the individual layers. The shift and modification of the absorbance, as well as for the E_{gap}, are discussed in detail later.

Concerning the reflectance, the curves of as dep. samples showed a complementary behavior with respect to their direct transmittance, a maximum of R_{tot} at minimum of T_{dir} and vice versa. The double stack showed total reflection lower than 27% while PCS lower than 25%.

After the thermal treatment, the PCS showed the same reflectance values in NIR range and a reduction from 700 nm to lower wavelength, with the larger decrease in the UV range (values until to 7%). At the same time, also a slight shift of the peak value (at ~ 24%) towards lower wavelength was observed. The double stack after the annealing showed a reduction in the whole wavelength range, with a big decrease in the UV and NIR ranges and with reflectance values were lower than 23%.

Fig. 8 shows the Tauc plots of all samples, used to estimate their optical band-gap, E_{gap}. Since both AZO and IZrO are wide direct band-gap transparent semiconductors, we used the Tauc's law (2) for direct transitions of electrons between valence band and conduction band of the material. The law is founded on an energy-dependent absorption coefficient α following the equation [48]:

$$(E\alpha)^2 = B(E - E_{gap}) \tag{2}$$

The E_{gap} value can be extrapolated by the intercept of the linear fit, calculated in the linear portion of the plot, with the E axis. In this equation, α is the absorption coefficient, E is the energy of photons, B is the Tauc coefficient and E_{gap} the band-gap of the material.

The value of α in our samples was obtained by the following equation
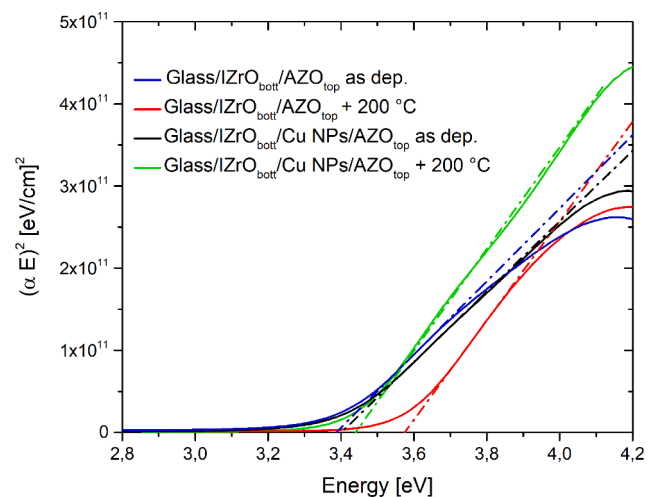
Fig. 8. Tauc plots and calculated linear fits of Glass/IZrO_bott/AZO_top and Glass/IZrO_bott/Cu NPs in acetone/AZO_top, as deposited and after a thermal annealing.

[49]:

$$\alpha_{PCS} = \frac{1}{d_{PCS}} In \frac{T_{Glass} \, (1 - R_{PCS})}{T_{PCS}} \tag{3}$$

Where T_{Glass} is the direct transmittance of the uncovered glass substrate, while d_{PCS}, T_{PCS} and R_{PCS} are the thickness, direct transmittance and specular reflectance of the samples, respectively. As we observed in our previous research [34–35], here we confirm the same trend for the as deposited samples, that is the transparent electrode with the lowest E_{gap} imposes its energy band-gap to the whole structure. Indeed, both samples show the E_{gap} value of AZO, see Table 1.

After the thermal annealing at 200 °C we observed a different behaviour because of the Cu NPs between the two transparent electrodes. If we examine the double stack after the annealing, the threshold in the direct transmittance moves towards lower wavelength, which means that the E_{gap} of sample increases, from 3.38 to 3.57 eV. The improvements in the transmission and the increase of E_{gap} are strictly related to the annealing, because it promotes the doping of Al and Zr in their metal oxides, the material crystallization and the reduction of the crystalline defects [36,50–55]. Also the reduction of R_{tot} and absorbance, especially in the UV range, are connected to these effects, while the presence of Cu NPs between the transparent electrodes modified the evolution after the thermal annealing. In this case the annealing causes: (i) a lower increase in the energy band-gap with respect to the double stack, from 3.39 to 3.43 eV; (ii) a reduction in the diffused transmittance in the whole wavelength range; (iii) a reduction in the total reflectance and absorbance (especially in the UV range). On one hand, the improvements of the E_{gap}, the reduction in R_{tot} and absorbance are related to annealing and its effects (doping, less defects and better crystallinity) on the structure; on the other hand the small increase in the E_{gap} and the reduction on T_{diff} could be related to copper diffusion towards AZO and IZrO. Although, the annealing was performed at low temperature and for short time, copper diffusion inside the metal oxide, both AZO and IZrO, could bring copper impurities (mainly as acceptors) in ZnO or In_2O_3 that lead to narrowing of the E_{gap} and, at the same time, a modification of Cu NPs, so decreasing the scattering of nanoparticles with T_{diff}. [36,56–61]. Subsequently, we show, although slight modifications have occurred from an optical point of view, that this type of impurity does not give any contribution or modification from an electrical point of view, especially if we compare the behavior, in terms of sheet resistance, of the composite film and the double film AZO/IZrO after annealing.

Regarding the sheet resistance, R_{sh} (4), of all samples and single layers [36] was measured at room temperature and reported in Table 1.

$$R_{sh} = \frac{\rho}{d} \tag{4}$$

$$\rho = \frac{1}{n_e \, e \, \mu_e} \tag{5}$$

where d is the thickness of film, ρ resistivity of film, n_e, e and μ_e are electrons's density, charge and mobility respectively.

The R_{sh} of the different structures, both with Cu NPs and without Cu NPs, can be calculated considering the bottom IZrO and the top AZO thin film as two resistors connected in parallel (6) [47]:

$$\frac{1}{R_{Sh, \; System}} = \frac{1}{R_{sh, \; bott \; IZrO}} + \frac{1}{R_{Sh, \; top \; AZO}} \tag{6}$$

This is based on the consideration that Cu NPs, with various sizes, randomly and uniformly distributed on bottom IZrO, do not constitute a continuous or worm-like thin film, therefore they do not give a contribution to electrical conduction. In any case, if effects like quantum mechanical tunneling among Cu NPs and/or the thermionic electron emission, in the bottom IZrO and top AZO thin films, might be take place, they would be negligible compared to the conduction taking place

in IZrO thin films.

This means that if we have two transparent electrodes with remarkable difference in R_{sh} values, the R_{sh} of the structure mainly depends on the transparent electrode with the lowest R_{sh}.

AZO layer, deposited by RF magnetron sputtering at room temperature, showed a very high value of R_{sh}, around 10^6 Ω/sq [34]. This value depends on different factors such as: film thickness, sputtering deposition parameters, deposition temperature, post-deposition annealing temperature and Al doping. In particular, we observed that our AZO showed a symmetric granular structure related to highly (0 0 2) textured columnar polycrystalline film with a wurtzite structure [50].

On the contrary, IZrO layer deposited at room temperature showed low sheet resistance of about 200–300 Ω/sq. Similarly to AZO, IZrO sheet resistance depends on several factors both during and after the deposition itself. In particular, zirconium introduces donor levels above the minimum of In_2O_3 conduction band that, at room temperature, can be activated supplying electron with high mobility μ_e. [51–55]. This explains the low R_{sh} despite room temperature synthesis. If we consider the double stack and PCS deposited at room temperature, as expected, due to the great difference in R_{sh} values of transparent electrode, the sheet resistance of both structures was controlled by IZrO layer with its R_{sh} of about 250 Ω/sq.

After the thermal annealing at 200 °C, we observed an improvement by a factor 4, for both structures, as the sheet resistance goes down to 79 Ω/sq. The reduction of one order of magnitude is related to the shallow thermal annealing, at 200 °C for 30 min, which is too low to significantly enhance the electrical performance of AZO, no more than $1.3 \; 10^4$ Ω/sq (AZO at 300 °C [34]), but it is enough to boost the IZrO electrical performance. Concerning the last assertion, XRD measurements on IZrO thin film, see figure S5, showed after an annealing at 200 °C a clear transition from amourphous (deposited at room temperature) to crystalline phase. If compared to pristine crystalline In_2O_3 XRD diffraction peaks [36], the relative peaks confirm the preferred orientation towards the (2 2 2) plane of our IZrO, in agreement to the In_2O_3 bixbyite structure. Moreover, Van der Pauw measurements pointed out that the improvement of the sheet resistance is motivated by increased electron concentration and hall mobility, up to $2.49 \; 10^{15}$ electrons/cm^2 and 31.5 cm^2/V s respectively.

The surface morphology of our best PCS made of "IZrObot/Cu NPs in acetone/AZO$_{top}$ + 200 °C", was investigated by atomic force microscopy (AFM) as shown in figure S6. The composite film exhibits a surface roughness values around 7 nm, in terms of Root Mean Square (RMS), which was compatible with the roughness observed in the cross section SEM image in Fig.1b.

In order to compare the electrical and optical performances, both should be as large as possibile for photovoltaic applications, of our best PCS with different transparent and conductive materials (as a function of kind of material, the thickness, deposition conditions and other details) used in solar cells or optoelectronic applications, we considered the Haacke's figure of merit. It was defined as FoM$_H$ = T^{10}/R$_{sh}$ [47], where R$_{sh}$ and T are the sheet resistance and the total transmittance of the corresponding transparent and conductive materials.

We calculated the FoM$_H$ value evaluating T in three different conditions:

i) Total transmittance (T$_{direct}$ + T$_{diffused}$) at 550 nm, T$_{Tot, \; 550}$ = 79.4 %;

ii) Mean value of total transmittance in Vis range, $<$T$_{Tot}>_{Vis}$ = 83.4 %;

iii) Mean value of total transmittance in Vis-NIR range, $<$T$_{Tot}>_{Vis-NIR}$ = 84.2 %;

because the optimal conditions, especially for our application in tandem solar cell, can be reached in wider wavelengths range than the 550 nm value typically used [47].

For these three conditions we obtained, respectively: FoM$_{H,550}$ = 1.3 10^{-3} Ω^{-1}; FoM$_{H,Vis}$ = 2.1 10^{-3} Ω^{-1}; FoM$_{H,Vis-NIR}$ = 2.3 10^{-3} Ω^{-1}. As expected, due to our PCS was optimized to show higher total

transmittance from visible to NIR range; with the same R_{sh}, increasing the mean value of transmittance the FoM$_H$ improves. Moreover, if we merely add to the mean value of the total transmittance the contribution loses in the glass substrate, a mean value of 8% from 400 to 1100 nm, see figure S7, because in the literature, commonly, the FoM$_H$ value was evaluated for free-standing films [47,62], we could achieve value of FoM$_{H,\ Vis-NIR}$ = 0.6 10^{-2} Ω^{-1}.

The last point is noteworthy because commonly the figure or merits are calculated for free-standing films [47,62] whereas in the real application a substrate, holder or encapsulation is required, e.g. superstrate configuration or glass encapsulation.

Finally, if we compare our best FoM$_H$ with the FoM reported in literature [37,62,63], we can conclude that our best PCS is competitive with the transparent electrodes reported in literature. Especially, if it takes into consideration that our PCS has got a total thickness of 150 nm, easy preparation/production, no special processing/treatment are requested but a slight and short thermal annealing at 200 °C for 30 min and all optical data included the glass substrate's contribution.

4. PCS in tandem solar cell: IQE characterization

Internal quantum efficiency (IQE) measurement is an effective method to analyze solar cells' behavior over a specific wavelength range. It measures the number of photons that essentially enter in the solar cell and the number of electrons generated and collected by the external electrodes. Differently from the external quantum efficiency (EQE), it does account for optical losses such as the reflection. The relation between EQE and IQE is [6,64]:

$$IQE(\lambda) = \frac{EQE(\lambda)}{(1-R)} = \frac{Electrons\ out}{Absorbed\ photons} \qquad (7)$$

Fig. 9 displays the IQE of tandem solar cells with the double stack and PCS as front electrodes, both as deposited and after thermal annealing. Starting from the as deposited structures, we observed higher performance for PCS compared to double stack, from ∼ 530 nm to NIR range, with IQE values ranging from 40% to 75% in Vis-NIR wavelength range. The better performance of PCS, as compared to the double stack, can be related to the higher values of T_{direct} and T_{diff}, while the same performances from 400 nm to UV range are related to the unchanged E_{gap} of the structures and the parasitic absorption losses in solar cells.

On the other hand, these losses are lower in NIR range thanks to the light scattering due to Cu NPs. Incident NIR photons penetrate in solar

cell with different depths compared to UV photons: in fact, UV with shorter wavelengths (higher energy) are quickly absorbed in the first layers of solar cell, i.e. PCS (especially if $E_{photon} > E_{gap}$), depletion region and p-type doped α-Si:H. Moreover, among optical losses, we have to account for the reflected light that has been lost. After the thermal annealing, the IQE of both samples showed great improvements: in particular, solar cell with PCS showed IQE values from 52 to 89 % in Vis-NIR wavelength ranges. These improvements are related to lower R_{sh}, higher T_{direct} and lower $R_{tot.}$ Lower sheet resistance helps collecting more photogenerated carriers. Moreover, the thermal annealing allows for better electrical connection between PCS and the absorber layer. In addition, the slight enhancement in T_{direct} and E_{gap} with the lower R_{tot}, especially in UV range, contributed to increase the IQE in UV–VIS range and up to about 1010 nm. The higher E_{gap} determined the shift of the absorption edge to lower wavelengths, enlarging the absorption window of solar cell. Even though the double stack showed higher E_{gap} than PCS, the parasitic absorption losses and the differences in absorbance, T_{dir}, R_{tot}, led to the same absorption edge. Finally, if we observe the behavior of T_{diff}, before and after the thermal annealing, the reduction of values from 9.5 to 3 % to 6–2.5% in Vis-NIR, and the otherimprovements, produced a little enhancement from 950 nm to higher wavelengths; on the other hand, it contributed to higher IQE values in the Vis-NIR range, as compared to the annealed double stack.

5. Conclusions

Cu nanoparticles produced by Laser ablation in liquid of Cu target, using a 1064 nm nanosecond pulsed laser in acetone and methanol, have shown, thanks to different analyses such as XRD, XPS, HR-TEM, EELS and EDX in STEM configuration, a metallic nature without amorphous carbon or copper oxides shells. Cu NPs, both in acetone and methanol, showed a spherical shape with two families of different size: smaller than 10 nm and larger than 10 nm in diameter. In particular, Cu NPs in acetone showed most representative radii of $x_p = 2.7$ nm and $x_p = 15$ nm, respectively, while Cu NPs in methanol showed most representative radii of $x_p = 1.7$ nm and $x_p = 31$ nm. Moreover, the smaller nanoparticles were more numerous than the larger ones.

Then, Cu nanoparticles produced in solvents were embedded between IZrO$_{bottom}$ and AZO$_{top}$ transparent electrodes with the configuration Glass/IZrO$_{bott}$/Cu NPs/AZO$_{top}$. The electro-optical performance of these structures showed a strong dependence on the thermal annealing (200 °C, 30 min, N$_2$ atmosphere) and type of copper nanoparticles embedded in transparent electrodes. The optimized structure made of Glass/IZrO$_{bott}$/Cu NPs in acetone/AZO$_{top}$ showed best electro-optical performance as plasmonic and conductive structure for photovoltaic application: sheet resistance value of 79 Ω/sq, E_{gap} of 3.43 eV, with a transmittance mean value of ∼ 79 % and diffused transmittance between 2.5% and 6% in Vis-NIR range.

Finally, the performance of the optimized PCS was tested measuring the internal quantum efficiency of a tandem solar cell (a-Si:H/c-Si), where the PCS was deposited on the front of the solar cell, resulting in quantu efficiencies as high as to 89%. In particular, the strength of this result lies in obtaining these values in a not optimized solar cells system, but a very simple architecture made of PCS, absorber layer and a metal back contact.

Low cost and abundant natural metal resources, with their utilization as metal nanostructures for enhancing solar cell performance, holds tremendous potential for the advancements of photovoltaic technology. Therefore, we believe that these results can contribute to the ongoing research and development in this field, driving towards high-efficiency, cost-effective, and eco-friendly solar cells that can accelerate the global adoption of renewable energy for a more sustainable and green future for the next generations to come.
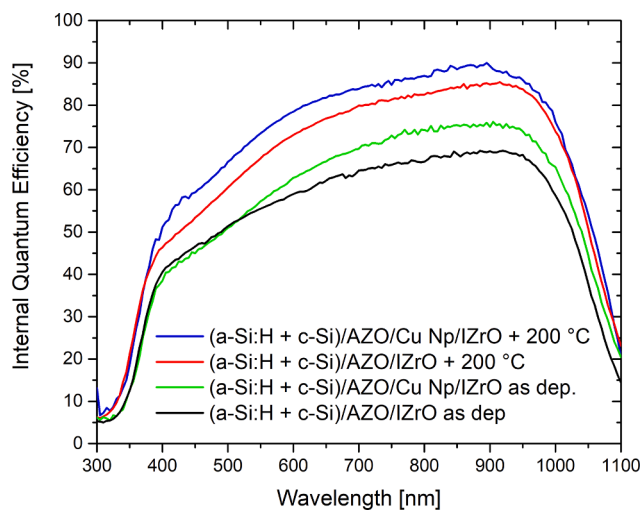

Fig. 9. Internal quantum efficiency of tandem solar cell (a-Si:H/c-Si) with the double stack and the PCS as front electrodes, both as deposited and after a thermal annealing at 200 °C for 30 min.

Funding

This work was supported by the project "Programma di ricerca di ateneo UNICT 2020-22 linea 2" of the University of Catania, Italy. This work was partially funded by European Union (Next Generation EU), through the MUR-PNRR project SAMOTHRACE (Grant No. ECS00000022).

CRediT authorship contribution statement

Stefano Boscarino: Conceptualization, Writing – original draft, Investigation, Data curation, Formal analysis, Supervision, Writing- review and editing. **Valentina Iacono:** Investigation. **Andrea Lo Mastro:** Investigation, Writing- review and editing. **Silvia Scalese:** Investigation, Writing- review and editing. **Simona Boninelli:** Investigation, Writing- review and editing. **Antonino Scandurra:** Investigation, Writing- review and editing. **Guglielmo Giudo Condorelli:** Investigation. **Roberto Corso:** Investigation. **Salvatore Lombardo:** Resources. **Riccardo Reitano:** Resources. **Antonio Terrasi:** Writing- review and editing, Funding acquisition, Resources. **Maria Grazia Grimaldi:** Funding acquisition, Resources. **Francesco Ruffino:** Conceptualization, Writing- review and editing, Supervision, Funding acquisition, Resources.

Declaration of competing interest

The authors declare that they have no known competing financial interests or personal relationships that could have appeared to influence the work reported in this paper.

Data availability

Data will be made available on request.

Acknowledgments

The authors thank the Bio-nanotech Research and Innovation Tower (BRIT) laboratory of the University of Catania (Grant No. PONa3_00136 financed by the MIUR) for the Smartlab diffractometer facility and Professor G. Malandrino (unict) for kind availability related to XRD measurements.

The authors thank Dott. M. Micali for providing IZrO XRD analysis.

Appendix A. Supplementary data

Supplementary data to this article can be found online at https://doi.org/10.1016/j.apsusc.2024.159547.

References

[1] Comunication from the commission to the European parliament, the council, the European economic and social committee and the committee of the regions. EU Solar Energy Strategy – Brussels – 18.05.2022.

[2] European Commission—Press Release. European Green Deal: EU Agrees Stronger Rules to Boost Energy Efficiency. Available online: https://ec.europa.eu/commission/presscorner/detail/en/ip_23_1581 (accessed on 1 August 2023).

[3] The White House: Office of the Press Secretary. Treasury Releases New Guidance to Drive Clean Energy Investment to America's Energy Communities. Available online: https://www.whitehouse.gov/cleanenergy/clean-energy-updates/2023/04/04/treasury-releases-new-guidance-to-drive-clean-energy-investment-to-americas-energy-communities/ (accessed on 1 Agust 2023).

[4] United Nations Framework Convention on Climate Change. New Mechanism Provides a Key Tool for Countries to Meet Their Climate Goals. Available online: https://unfccc.int/news/new-mechanism-provides-a-key-tool-for-countries-to-meet-their-climate-goals (accessed on 1 august 2023).

[5] https://fridaysforfuture.org/ (accessed on 1 august 2023).

[6] R. Saive, Light trapping in thin silicon solar cells: A review on fundamentals and technologies, Prog. Photovolt. Res. Appl. 29 (2021) 1125–1137, https://doi.org/10.1002/pip.3440.

[7] O. Agustsson, A. Schutz, T. Oyama, J. Schotsaert, O. Mai, Development of textured TCO for thin film silicon solar cells, Glass Performance Days Conference (2009) 508–511.

[8] W.L. Bailey, M.G. Coleman, C.B. Harris, I.A. Lesk, United States Patent: 4137123 - Texture etching of silicon: method, 1979.

[9] P. Campbell, M.A. Green, Light trapping properties of pyramidally textured surfaces, J. Appl. Phys. 62 (1987) 243–249, https://doi.org/10.1063/1.339189.

[10] P. Campbell, M.A. Green, High performance light trapping textures for monocrystalline silicon solar cells, Sol. Energy Mater. Sol. Cells 65 (2001) 369–375, https://doi.org/10.1016/S0927-0248(00)00115-X.

[11] D.J. De Aberasturi, A.B. Serrano-Montes, L.M. Liz-Marzán, Modern applications of Plasmonic nanoparticles: from energy to health, Adv. Optical Mater. 3 (2015) 602–617, https://doi.org/10.1002/adom.201500053.

[12] U. Qazi, R. Javaid, A review on metal nanostructures: preparation methods and their potential applications, Adv. Nanopart. 5 (2016) 27–43, https://doi.org/10.4236/anp.2016.51004.

[13] R. Jiang, B. Li, C. Fang, J. Wang, Metal/Semiconductor hybrid nanostructures for plasmon-enhanced applications, Adv. Mater. 26 (2014) 5274–5309, https://doi.org/10.1002/adma.201400203.

[14] M. Fernández-Arias, M. Boutinguiza, J. Del Val, C. Covarrubias, F. Bastias, L. Gómez, M. Maureira, F. Arias-González, A. Riveiro, J. Pou, Copper nanoparticles obtained by laser ablation in liquids as bactericidal agent for dental applications, Appl. Surf. Sci. 507 (2020) 145032, https://doi.org/10.1016/j.apsusc.2019.145032.

[15] J. Liu, H. He, D. Xiao, S. Yin, W. Ji, S. Jiang, D. Luo, B. Wang, Y. Liu, Recent advances of plasmonic nanoparticles and their applications, Materials 11 (2018) 1833, https://doi.org/10.3390/ma11101833.

[16] F. Parveen, B. Sannakki, M.V. Mandke, H.M. Pathan, Copper nanoparticles: Synthesis methods and its light harvesting performance, Sol. Energy Mater. Sol. Cells 144 (2016) 371–382, https://doi.org/10.1016/j.solmat.2015.08.033.

[17] A. Maier Stefan, Plasmonics: Fundamentals and Applications. Springer, NY, 2007. https://doi.org/10.1007/0-387-37825-1.

[18] Kitcometals. http://www.kitcometals.com/charts & https://www.kitco.com/charts (accessed on 06/09/2023).

[19] NASDAQ. https://www.nasdaq.com/market-activity (accessed on 06/09/2023).

[20] P. Zheng, H. Tang, B. Liu, S. Kasani, L. Huang, N. Wu, Origin of strong and narrow localized surface plasmon resonance of copper nanocubes, Nano Res. 12 (2019) 63–68, https://doi.org/10.1007/s12274-018-2178-6.

[21] K. Sugawa, T. Tamura, H. Tahara, D. Yamaguchi, T. Akiyama, J. Otsuki, Y. Kusaka, N. Fukuda, H. Ushijima, Metal-enhanced fluorescence platforms based on plasmonic ordered copper arrays: wavelength dependence of quenching and enhancement effects, ACS Nano 7 (2013) 9997–10010, https://doi.org/10.1021/nn403925d.

[22] G.H. Chan, J. Zhao, E.M. Hicks, G.C. Schatz, R.P. Van Duyne, Plasmonic properties of copper nanoparticles fabricated by nanosphere lithography, Nano Lett. 7 (2007) 1947–1952, https://doi.org/10.1021/nl070648a.

[23] Y. Fang, Z. Cheng, S. Wang, H. Hao, L. Li, S. Zhao, X. Chu, R. Zhu, Effects of oxidation on the localized surface plasmon resonance of Cu nanoparticles fabricated via vacuum coating, Vacuum 184 (2021) 109965, https://doi.org/10.1016/j.vacuum.2020.109965.

[24] M.B. Gawande, A. Goswami, F. Felpin, T. Asefa, X. Huang, R. Silva, X. Zou, R. Zboril, R.S. Varma, Cu and Cu-Based nanoparticles: synthesis and applications in catalysis, Chem. Rev. 116 (2016) 3722–3811, https://doi.org/10.1021/acs.chemrev.5b00482.

[25] R.M. Tilaki, A. Iraji zad, S.M. Mahdavi, Size, composition and optical properties of copper nanoparticles prepared by laser ablation in liquids, Appl. Phys. A 88 (2007) 415–419, https://doi.org/10.1007/s00339-007-4000-2.

[26] N. Bhalla, A. Jain, Y. Lee, A.Q. Shen, D. Lee, Dewetting Metal Nanofilms—Effect of Substrate on Refractive Index Sensitivity of Nanoplasmonic Gold, Nanomaterials 9 (2019) 1530, https://doi.org/10.3390/nano9111530.

[27] C.V. Thompson, Solid-state dewetting of thin films, Annu. Rev. Mater. Res. 42 (2012) 399–434, https://doi.org/10.1146/annurev-matsci-070511-155048.

[28] P.K. Baruah, A.K. Sharma, A. Khare, Role of confining liquids on the properties of Cu@Cu$_2$O nanoparticles synthesized by pulsed laser ablation and a correlative ablation study of the target surface, RSC adv. 9 (2019) 15124–15139, https://doi.org/10.1039/C9RA00197B.

[29] P. Liu, H. Wang, X. Li, R. Muchen, H. Zeng, Localized surface plasmon resonance of Cu nanoparticles by laser ablation in liquid media, RSC Adv. 5 (2015) 79738–79745, https://doi.org/10.1039/C5RA14933A.

[30] R. Rawat, A. Tiwari, N. Arun, S.V.S.N. Rao, A.P. Pathak, A. Tripathi, Solvents effect on the morphology and stability of Cu/CuO nanoparticles synthesized at high fluence laser ablation, ChemistrySelect 4 (2019) 10471–10482, https://doi.org/10.1002/slct.201902344.

[31] C.C. Crane, F. Wang, J. Li, J. Tao, Y. Zhu, J. Chen, Synthesis of Copper-Silica Core–Shell Nanostructures with Sharp and Stable Localized Surface Plasmon Resonance, J. Phys. Chem. C 121 (2017) 5684–5692, https://doi.org/10.1021/acs.jpcc.6b11891.

[32] C. Huang, G. Kumar, G.D. Sharma, F. Chen, Plasmonic effects of copper nanoparticles in polymer photovoltaic devices for outdoor and indoor applications, Appl. Phys. Lett. 116 (2020) 253302, https://doi.org/10.1063/5.0010427.

[33] P. Shen, Y. Liu, Y. Long, L. Shen, B. Kang, High-Performance Polymer Solar Cells Enabled by Copper Nanoparticles-Induced Plasmon Resonance Enhancement, J. Phys. Chem. C 120 (2016) 8900–8906, https://doi.org/10.1021/acs.jpcc.6b02802.

[34] S. Boscarino, M. Censabella, M. Micali, M. Russo, A. Terrasi, M.G. Grimaldi, F. Ruffino, Morphology, electrical and optical properties of Cu nanostructures

embedded in AZO: a comparison between dry and wet methods, Micromachines 13 (2022) 247, https://doi.org/10.3390/mi13020247.

[35] S. Boscarino, V. Iacono, A. Lo Mastro, F. Tringali, A. Terrasi, M.G. Grimaldi, F. Ruffino, Plasmonic and Conductive Structures of TCO Films with Embedded Cu Nanoparticles, Int. J. Mol. Sci. 23 (2022) 11886, https://doi.org/10.3390/ijms231911886.

[36] D.S. Ginley, H. Hosono, D.C. Paine, Handbook of Transparent Conductors, Springer, Berlin, 2010.

[37] K. Ellmer, Past achievements and future challenges in the development of optically transparent electrodes, Nature Photon 6 (2012) 809–817, https://doi.org/10.1038/nphoton.2012.282.

[38] S. Barcikowski, V. Amendola, G. Marzun, C. Rehbock, S. Reichenberger, D. Zhang, B. Gökce, Handbook of Laser Synthesis of Colloids, Universität Duisburg-Essen (2016).

[39] ImageJ – Image Processing and Analysis in Java. https://imagej.nih.gov/ij/index.html.

[40] C.G. Granqvist, R.A. Buhrman, Log-normal size distributions of ultrafine metal particles, Solid State Commun. 18 (1976) 123–126, https://doi.org/10.1016/0038-1098(76)91415-0.

[41] C. Lo Pò, V. Iacono, S. Boscarino, M.G. Grimaldi, F. Ruffino, Monte Carlo Approach to the evaluation of nanoparticles distribution from the analysis of UV-Vis_NIR spectra, Micromachines 14 (2023) 2208, https://doi.org/10.3390/mi14122208.

[42] J.F. Moulder, W.F. Stickle, P.E. Sobol, Handbook of X-ray photoelectron spectroscopy, Perkin-Elmer Corporation, Physical Electronics Division, 1992.

[43] A. Scandurra, M. Censabella, S. Boscarino, M.G. Grimaldi, F. Ruffino, G. G. Condorelli, G. Malandrino, Solid state fabrication of Cu₂O/CuO-hydroxide nanoelectrode array onto graphene paper by thermal dewetting for high sensitive detection of glucose, Phys. Status Solidi A 218 (2021) 2100389, https://doi.org/10.1002/pssa.202100389.

[44] PDF card no.: 00-004-0836 quality: s.

[45] PDF card no.: 00-089-5895 quality: c.

[46] PDF card no.: 00-077-0199 quality: c.

[47] C. Guillén, J. Herrero, TCO/metal/TCO structures for energy and flexible electronics, Thin Solid Films 520 (2011) 1–17, https://doi.org/10.1016/j.tsf.2011.06.091.

[48] J. Tauc, R. Grigorovici, A. Vancu, Optical Properties And Electronic Structure of Amorphous Germanium, Phys. Status Solidi B 15 (1966) 627–637, https://doi.org/10.1002/pssb.19660150224.

[49] S. Mirabella, R. Agosta, G. Franzó, I. Crupi, M. Miritello, R. lo Savio, M.A. Di Stefano, S. Di Marco, F. Simone, A. Terrasi, Light absorption in silicon quantum dots embedded in silica, J. Appl. Phys. 106 (2009), 103505.

[50] S. Boscarino, G. Torrisi, I. Crupi, F. Ruffino, A. Terrasi, Ion irradiation of AZO thin films for flexible electronics, Nucl. Instrum. Methods Phys. Res., Sect. B 392 (2017) 14–20, https://doi.org/10.1016/j.nimb.2016.11.037.

[51] J. Xu, J.B. Liu, B.X. Liu, S.N. Li, S.H. Wei, B. Huang, Design of n-type transparent conducting oxides: the case of transition metal doping in In₂O₃, Adv. Electron. Mater. 4 (2018) 1700553, https://doi.org/10.1002/aelm.201700553.

[52] Y.C. Liang, Y.C. Liang, Physical properties of low temperature sputtering-deposited zirconium-doped indium oxide films at various oxygen partial pressures, Appl. Phys. A 97 (2009) 249–255, https://doi.org/10.1007/s00339-009-5214-2.

[53] E. Rucavado, F. Landucci, M. Döbeli, Q. Jeangros, M. Boccard, A. Hessler-Wyser, C. Ballif, M. Morales-Masis, Zr-doped indium oxide electrodes: Annealing and thickness effects on microstructure and carrier transport, Phys. Rev. Materials 3 (2019) 084608, https://doi.org/10.1103/PhysRevMaterials.3.084608.

[54] B. Aissa, Y. Zakaria, A.R. Shetty, A. Samara, C. Broussillou, High Electron-Mobility of a Transparent and Conductive Zr-Doped In₂O₃Deposited by Reactive Magnetron Sputtering, Conf. Rec. IEEE Photovolt. Spec. Conf. 40 (2021) 71–73, https://doi.org/10.1109/PVSC43889.2021.9518643.

[55] M. Morales-Masis, E. Rucavado, R. Monnard, L. Barraud, J. Holovsky, Y. Despeisse, M. Boccard, C. Ballif, Highly Conductive and Broadband Transparent Zr-Doped In₂O₃ as Front Electrode for Solar Cells, IEEE J. Photovoltaics 8 (2018) 1202–1207, https://doi.org/10.1109/JPHOTOV.2018.2851306.

[56] Z.N. Kayani, S. Iram, R. Rafi, Effect of Cu Doping on The Structural, Magnetic and Optical Properties of ZnO Thin Films, Appl. Phys. Mater. Sci. Process. 124 (2018) 468–470, https://doi.org/10.1007/s00339-018-1886-9.

[57] B.K. Das, T. Das, K. Parashar, Structural, Bandgap Tuning and Electrical Properties of Cu Doped ZnO Nanoparticles Synthesized by Mechanical Alloying, J. Mater. Sci. Mater. Electron. 28 (2017) 15127–15134, https://doi.org/10.1007/s10854-017-7388-2.

[58] M. Fang, C.M. Tang, Z.W. Liu, Microwave-Assisted Hydrothermal Synthesis of Cu Doped ZnO Single Crystal Nanoparticles with Modified Photoluminescence and Confirmed Ferromagnetism, J. Electron. Mater. 47 (2018) 1390–1396, https://doi.org/10.1007/s11664-017-5928-4.

[59] M. Chakraborty, A. Ghosh, R. Thangavel, Experimental and Theoretical Investigations of Structural and Optical Properties of Copper Doped ZnO Nanorods, J. Sol-Gel Sci. Technol. 74 (2015) 756–764, https://doi.org/10.1007/s10971-015-3660-1.

[60] S.A. Ahmed, Effect of Annealing Temperature and Dopant Concentration on The Structure, Optical, and Magnetic Properties of Cu-doped ZnO Nanopowders, J. Mater. Sci. Mater. Electron. 28 (2017) 3733–3739, https://doi.org/10.1007/s10854-016-5981-4.

[61] F.Y. Ran, M. Tanemura, Y. Hayashi, T. Hihara, Effect of Substrate Temperature on the Room-Temperature Ferromagnetism of Cu-doped ZnO films, J. Cryst. Growth. 31 (2009) 4270–4274, https://doi.org/10.1016/j.jcrysgro.2009.07.008.

[62] A.I. Hofmann, E. Cloutet, G. Hadziioannou, Materials for Transparent Electrodes: From Metal Oxides to Organic Alternatives, Adv. Electron. Mater. 10 (2018) 1700412, https://doi.org/10.1002/aelm.201700412.

[63] S. Ghosh, A. Mallick, B. Dou, M.F.A.M. van Hest, S.M. Garner, D. Basak, A novel blanket annealing process to achieve highly transparent and conducting Al doped ZnO thin films: Its mechanism and application in perovskite solar cells, Sol. Energy 174 (2018) 815–825, https://doi.org/10.1016/j.solener.2018.09.017.

[64] M.Z. Farah Khaleda, B. Vengadaesvaran, N.A. Rahim, Chapter 18 - Spectral response and quantum efficiency evaluation of solar cells: a review. Energy Mater.: Fundament. Appl., Elsevier, 2021, Pages 525-566.